

Microspine Design for Additive Manufacturing

Paul Nadan¹, Dinesh K. Patel², Catherine Pavlov³, Spencer Backus⁴, and Aaron M. Johnson³

Abstract—Microspine grippers allow robots to ascend steep rocky slopes and cliff faces, enabling scientific exploration of exposed strata on Earth and other solar system bodies. Historically, the Shape Deposition Manufacturing (SDM) process has been used to fabricate multi-material suspensions for load-sharing among multiple microspines. We instead apply the Hybrid Deposition Manufacturing (HDM) process to microspine fabrication, and we further propose a novel 3D-printed microspine suspension design that can be manufactured via Fused Deposition Manufacturing (FDM) alone, using a single flexible material with an embedded fishhook. We use a model of microspine stiffness that allows designers to compensate for order-of-magnitude changes in material tensile modulus by adjusting geometric parameters of the design. The stiffness model and the FDM microspine design are validated through tensile testing, and mechanical properties of the HDM and FDM designs are compared against a standard SDM microspine design. We demonstrate that the FDM process can produce microspines with equivalent normal and axial stiffness and superior maximum load and fatigue response to SDM microspines, and discuss additional advantages of the FDM process for rapid prototyping and broader accessibility.

I. INTRODUCTION

Climbing robots can advance scientific exploration of our solar system by enabling access to exposed strata found on steep terrain that conventional wheeled rovers cannot reach, such as the cliff faces observed in Jezero and Victoria Craters on Mars, or lava tubes with vent openings on the Martian and lunar surfaces [1–4]. Robust, reliable adhesion to vertical or even overhanging surfaces can be achieved through the use of microspines, which use small, sharp hooks to take advantage of millimeter to sub-millimeter scale surface features. Unlike other adhesion mechanisms such as suction, magnetism, or dry adhesion, microspines are well-suited to the rough rock and cliff surfaces commonly encountered during planetary exploration [5–7].

While any individual microspine can only support a small force, a gripper comprising multiple microspines can support larger forces through load-sharing [8], Fig. 1. Flexible suspensions enable the microspines to move independently, individually catching on asperities as the gripper is dragged along a surface. These suspensions are typically made using

This work was supported by a NASA Space Technology Graduate Research Opportunities Award. A portion of this research was carried out at the Jet Propulsion Laboratory, California Institute of Technology, under a contract with the National Aeronautics and Space Administration (80NM0018D0004).

¹Robotics Institute, ²Human-Computer Interaction Institute, ³Mechanical Engineering, Carnegie Mellon University, Pittsburgh, PA 15213, USA, {pnadan, dineshpa, cpavlov, amj1}@andrew.cmu.edu

⁴Jet Propulsion Laboratory, California Institute of Technology, 4800 Oak Grove Drive M/S 82-105, spencer.backus@jpl.nasa.gov



Fig. 1. A simple gripper composed of nine 3D-printed microspines contained in a carriage. The gripper is shown supporting a 30N tangential load on a vertical cinder block surface. One can observe that individual microspines have translated relative to each other in order to catch on asperities and distribute the load between them.

Shape Deposition Manufacturing (SDM), a process in which alternating subtractive machining and casting steps produce a multi-material part containing both rigid and elastic elements [8]. This approach has proven extremely effective, and microspines made with SDM have been used on a wide range of climbing and perching robots [7,9–12].

However, the SDM process is time, labor, and equipment intensive due to long curing times and the use of CNC machine tools, with fabrication of new microspine designs taking multiple days of skilled work [11]. Additive manufacturing (AM), or 3D printing, offers potential improvements in all of these areas; parts can be produced quickly and cheaply with minimal human labor. Furthermore, additive manufacturing may allow for greater failure loads, longer life, or new designs with more complex geometry. In particular, Fused Deposition Manufacturing (FDM) printers are widely available, used by hobbyists and researchers alike, and offer low part costs and large batch sizes in comparison to other additive methods [13].

In this work, we introduce new fabrication techniques and a design model for microspines using two additive manufacturing approaches: Hybrid Deposition Manufacturing (HDM) and Fused Deposition Manufacturing (FDM). We then experimentally compare microspines made via SDM to those

made using these new methods. While the HDM method suffers from issues with delamination, we demonstrate that FDM achieves superior mechanical properties to SDM with significant reductions in manufacturing time, labor, and fabrication infrastructure. This makes additive manufacturing a valuable tool for rapid prototyping of microspine designs and increases the broader accessibility of microspine gripper technology. Section II describes the SDM, HDM, and FDM manufacturing processes in more detail, as well as current alternative approaches for microspine fabrication. Section III details the design process for applying HDM and FDM techniques to microspine fabrication, including a general model for tuning microspine stiffness through geometry. Section IV describes the mechanical testing procedure that was used to evaluate the performance of each microspine type, and Section VI analyzes the results of these experiments.

II. BACKGROUND AND RELATED WORK

The SDM process, developed in [14,15], can form multi-material parts with embedded components through alternating subtractive and additive steps. In [8], this process is applied to create microspines using hard and soft urethane polymers with embedded fishhooks. The procedure requires several steps. First, a cavity is cut into a machineable wax block using a CNC milling machine. At this point the fishhook is embedded into the part and the cavity is filled with hard urethane resin. After the urethane has cured, new cavities are cut into the part during a second CNC pass. These are filled with flexible urethane resin and allowed to cure, after which the finished microspine can be removed from the wax block.

The FDM process is an additive manufacturing technique based on filament extrusion [13,16]. This technique is simple, rapid, and low-cost, while its drawbacks include the appearance of layers, surface roughness, and minimum feature size. New materials with desired material properties like stiffness, strength, flexibility, conductivity are available [16–18]. Advances in multi-material printing using dual extruders facilitates fabrication of structures with complex geometries and overhangs [13]. This technique is commonly used in mechanisms such as grippers and compliant joints for a robot [17,19,20].

The HDM process combines elements of both SDM and FDM to produce multi-material parts [21]. One or more solid bodies are first 3D-printed and assembled together with a 3D printed mold. The cavities are then filled with a resin such as urethane, which is allowed to cure. Finally, the mold is discarded to leave the finished part. More complex parts can be built up by repetition of this process. A single monolithic printed part can even use sacrificial mold walls that are removed after casting to eliminate the need for a separate mold. HDM offers similar capability to SDM while reducing manufacturing effort and allowing overhanging features that are not possible with SDM alone.

A few alternative approaches to SDM have previously been used for microspine fabrication. Researchers in [22] developed fully metallic microspines that can function in

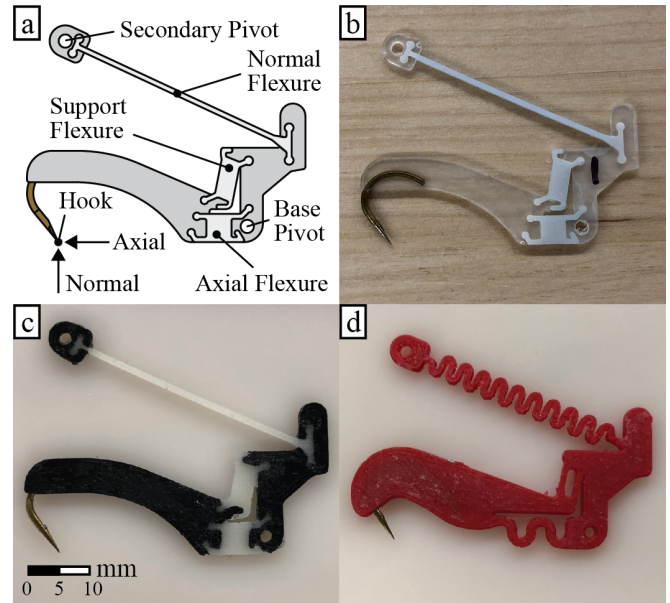


Fig. 2. a) Diagram of basic microspine geometry. b-d) Images of microspines fabricated using b) Shape Deposition Manufacturing, c) Hybrid Deposition Manufacturing, and d) Fused Deposition Manufacturing techniques.

space environments. These microspines use the bending of thin metal ribbons to provide desired stiffness properties. Subsequent work on metallic microspines in [23,24] instead used a serpentine ribbon geometry to achieve the desired stiffness. In [11], researchers developed rotary microspines that could be fabricated from a single material. They used cast urethane with a higher stiffness than conventional SDM microspines, which was rigid enough to allow embedding of the hook while also flexible enough to enable load-sharing. In [25,26], researchers embedded microspines at the ends of compliant, laser-cut acrylic and 3D-printed PLA legs. The higher material stiffness is compensated for by the length of the legs, but the materials used cannot provide sufficient compliance when scaled to the smaller form factor of most grippers. Another approach uses laser-cut sheets of soft and hard material that are then glued together along with a spine [27]. Other grippers have avoided the use of flexures entirely: the JPL-Nautilus gripper in [28] instead used springs and tendons for load sharing, and researchers in [29] used an array of spring-loaded, linearly constrained spines.

In this work we focus on multi-material microspines with elastic flexures as in [8] due to their widespread use and advantages such as multi-directional compliance and compact form factor.

III. MICROSPINE DESIGN

To allow a controlled comparison among manufacturing approaches, this section considers a typical SDM microspine design (Fig. 2b), originally used for the microspine gripper in [10], and details the design adjustments required to apply the HDM and FDM processes.

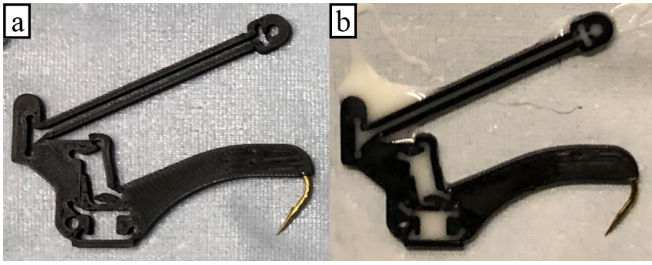


Fig. 3. HDM microspine manufacturing process. The 3D-printed rigid elements and break-away mold walls are shown a) prior to casting and b) immediately after casting.

A. SDM Microspine Design

The SDM microspines, following the design in [10], are cast from rigid Smooth-On Task 9 and flexible Smooth-On VytaFlex 60 urethane resins, with a Tiemco TMC300 #2 fishhook for the hook. This SDM microspine design is meant to provide relatively high axial stiffness (parallel to the surface) and low normal stiffness (into the surface), and to minimize rotation of the hook during loading. This is achieved using three separate elastic flexures, labeled in Fig. 2a. The axial flexure allows the microspine to stretch axially for load-sharing between microspines as they catch on different asperities. When stretched, the normal flexure applies a torque about the base pivot point that presses the hook against the surface. Lastly, the support flexure provides a vertical constraint that prevents the hook from rotating in plane as the microspine is axially loaded, thereby maintaining a constant contact angle between the hook and the surface [8].

B. HDM Microspine Design

The standard HDM process can be applied to microspines with minimal modification. In this work, PLA was used for the 3D-printed rigid material, and Vytaflex 60 was used for the cast flexible material. Thin, break-away mold walls were added to the design to contain the urethane during casting (Fig. 3a). As in [21], 0.1mm gaps were left in the design in between the break-away walls and the rest of the part. During the actual print the gaps are filled in due to the width of the extruder, but the programmed gaps reduce the strength of the connection for easier removal of the mold walls after casting. During printing, the 3D printer must be paused prior to the final layer, allowing a fishhook to be press-fit into the exposed cavity as in [25,26]. Using the PrusaSlicer slicing software it is straightforward to insert a pause into the program. After the print is resumed, the final layer will fully cover the hook.

The finished 3D-printed part is placed on a layer of adhesive tape to prevent leakage during casting. For best results, the same side of the microspine that was contacting the print bed should contact the tape because of its smoother surface finish. The flexible urethane casting process can then proceed as in the SDM approach (Fig. 3b), after which the mold walls can be removed (Fig. 2c).

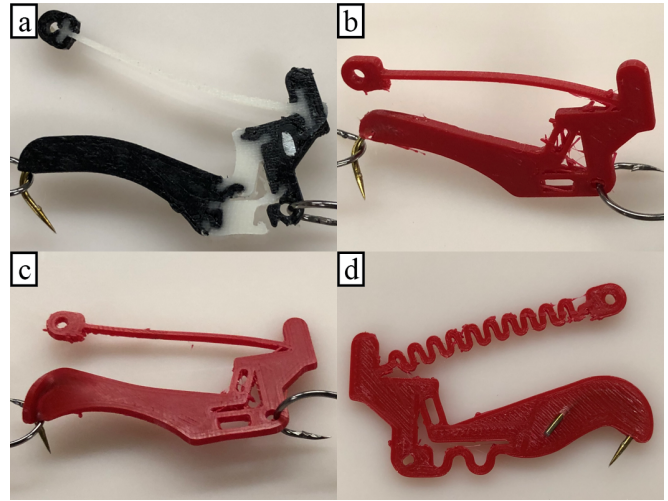


Fig. 4. Examples of failure modes encountered during microspine design. a) Delamination at the material interface of an HDM microspine. b) Insufficient material around hook, c) out-of-plane twisting, and d) hook tearing free of FDM microspines.

C. FDM Microspine Design

To further simplify fabrication and eliminate resin casting entirely, here we propose replacing the cast microspines with FDM microspines printed using a flexible thermoplastic polyurethane (TPU) filament. The challenge with this approach is that filaments with comparable Shore hardness to the flexible urethane are uncommon, difficult to work with, and only compatible with 3D printers capable of both multi-material printing and handling very flexible filaments. Instead, we propose the fabrication of microspines using a single material for both rigid bodies and elastic flexures. This approach requires significant changes to the microspine geometry, for which purpose we present a model of microspine stiffness as a function of material and geometric parameters.

One of the key advantages of the single-material approach is that there are no interfaces between different materials that can delaminate under load, as seen in Fig. 4a. While single-material metallic microspines were designed in [22–24], the use of a more flexible material allows for simpler microspine geometries and less precise manufacturing methods.

For the flexible filament, we selected NinjaFlex Cheetah, a TPU filament with 95A Shore hardness. The higher stiffness of the Cheetah filament allows the hook to be directly embedded in the flexible material, as in [11]. Using the original SDM microspine geometry, the flexible filament is less effective at constraining the fishhook and it is free to rotate out of plane (Fig. 4b). Extra material is added around the fishhook to address this, leaving less of the hook exposed.

Additionally, microspines made of a flexible filament have lower rigidity, which can manifest as out-of-plane twisting of the region between the hook and the axial flexure when the microspine is loaded (Fig. 4c). To compensate, a greater length of the fishhook shaft is embedded in the part. Load applied to the hook is transferred along the shaft of the hook to the axial flexure, so that no twisting moment can

occur. Due to the shape of the fishhook, this design change requires reducing the size of the cutout between the hook and base pivot, which was introduced in [10] to reduce interference with surface irregularities; however, this cutout was not present in prior microspine designs, so the larger size is not considered essential.

The cavity in which the hook is embedded must also be more carefully sized than in the case of HDM microspines; due to the softer material, any extra clearance around the fishhook may enable it to twist out of plane and tear through the side of the microspine (Fig. 4d).

Most significantly, the spring stiffness of all three flexures increases dramatically due to the increased tensile modulus of the material. This increase can be counteracted by changing the flexure geometry. In [30], the authors demonstrate that a serpentine ribbon geometry can reduce stiffness by multiple orders of magnitude. In our FDM microspine design, both the axial and normal flexures have been changed to serpentine geometries in order to enable a lower stiffness than the TPU material properties would allow in a rectilinear geometry. The relatively wide axial and supporting flexures of the original design each fully constrain translation and rotation in the flexure plane, while a serpentine flexure provides only a translation constraint along the flexure axis. Making both flexures serpentine would therefore leave one degree of freedom unconstrained. Instead, the axial tendon is made serpentine, while the supporting flexure is replaced with two narrow parallel flexures. The parallel flexures act as a 4-bar linkage to constrain both translation along their axis and rotation, so that in combination with the axial flexure the system remains fully constrained as in the original design. For a more general approach to flexure design, the Freedom and Constraint Topology (FACT) approach [31] provides a comprehensive mapping between desired motions and constraints.

We derive a linear elastic stiffness model for the two serpentine flexures and the support flexure in order to match the stiffness of the original SDM design at small displacements. Though nonlinear constitutive laws for viscoelastic materials [32] would better generalize to large displacements, these laws would require the measurement of additional material parameters and thus increase the difficulty of applying the model to new materials. Similarly, other approaches such as the Beam Constraint Model (BCM) [33] can account for elastokinematic nonlinearities at larger flexure displacements, but a linear approximation is sufficient for a relative comparison. For the axial and normal flexures, we use the serpentine ribbon model from [30] to select the flexure geometry. They define the ribbon geometry by the flexure width w , arc radius R , arm length l , and arc opening angle α , as shown in Fig. 5a, from which the stiffness of a given flexure design can be computed. According to their model, the reduction in stiffness is scale invariant and monotonic with smaller w/R , larger l/R , and larger α . We can use their model to compute

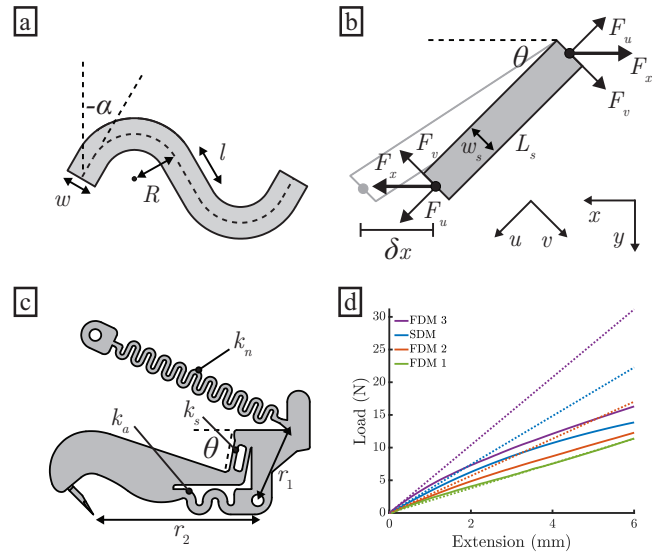


Fig. 5. a) Geometric parameters for a serpentine ribbon flexure, as defined in [30]. b) Diagram of an individual flexure subject to a tensile load F_u and bending load F_v caused by a lateral displacement δx . c) Labeled stiffness contributions of each flexure, as well as moment arms r_1 and r_2 and support flexure angle θ . d) Load-displacement curves (solid) for the SDM microspine design and three variations of the FDM microspine design, overlaid against linear model predictions (dotted). Legend entries are arranged in the same order as the curves. The SDM and FDM 2 results are averaged over 5 samples, while the FDM 1 and FDM 3 results are each based on a single trial.

the stiffness of the axial flexure (k_a) and normal flexure (k_n),

$$k_a = \frac{Ew_a h}{L_a} S \left(\frac{w_a}{R_a}, \frac{l_a}{R_a}, \alpha_a \right) \quad (1)$$

$$k_n = \frac{Ew_n h}{L_n} S \left(\frac{w_n}{R_n}, \frac{l_n}{R_n}, \alpha_n \right) \quad (2)$$

where subscripts a and n denote parameters of the axial and normal flexure respectively, L is the flexure length, h is the flexure thickness, E is the material tensile modulus, and S is the relative effective stiffness of a serpentine ribbon as derived in [30].

For the support flexure, we derive the stiffness of a flexure loaded at an angle relative to its axis. Here, we consider a support flexure of length L_s and width w_s , with its longitudinal axis rotated θ degrees from the horizontal x axis (Fig. 5b). With one end of the flexure fixed and the other rotationally constrained but free to translate, we apply a horizontal load F_x at the free end, such that the flexure experiences a horizontal deflection δx along the x axis. The load can be decomposed into a tensile force along the flexure's length due to axial elongation, F_u , and a shearing force perpendicular to the flexure due to bending, F_v , given by,

$$F_u = \frac{Ew_s h}{L_s} \delta x \cos \theta \quad (3)$$

$$F_v = \frac{12EI_s}{L_s^3} \delta x \sin \theta \quad (4)$$

where $I_s = \frac{w_s^3 h}{12}$ is the area moment of inertia.

We can then superimpose and project the resulting forces onto the axis of applied load to get the combined applied load F_x and compute the spring stiffness k_s for the support flexure along the axial direction of the microspine,

$$F_x = F_u \cos(\theta) + F_v \sin(\theta) \quad (5)$$

$$k_s = \frac{F_x}{\delta x} = \frac{Ew_s h}{L_s} \cos^2 \theta + \frac{12EI_s}{L_s^3} \sin^2 \theta \quad (6)$$

Applying this model to a microspine (Fig. 5c), the axial stiffness is determined by both the serpentine axial flexure and the support flexure, and the normal stiffness is determined by the normal flexure adjusted for the lever arm of the applied load. The overall microspine stiffness is then given by,

$$k_{axial} = k_a + n_s k_s \quad (7)$$

$$k_{normal} = k_n \left(\frac{r_1}{r_2} \right)^2 \quad (8)$$

where n_s is the number of support flexures and r_1 and r_2 are the moment arms about the base pivot of the normal flexure and the normal load, respectively (Fig. 5c). Normal compliance of the support and axial tendons is negligible compared to the compliance of the normal tendon, and thus not included for simplicity.

To validate this model, we produced three microspine designs with differing axial flexure geometry. The geometries were chosen to vary the predicted microspine axial stiffness while meeting space constraints. These three designs, along with a standard SDM microspine, were fabricated and axially loaded to measure stiffness as in Section IV. Geometric parameters and tensile modulus for each microspine design are given in Table I. The tensile modulus of the urethane resin was not published, so the 100% modulus was used as a substitute. For the FDM design we treat the support flexure as two thinner individual flexures. When entering dimensions into the model, it is important to account for changes in the part size during printing; we found that the width of each flexure increased by 0.3mm from the original design, and the height of the part increased by 0.1mm.

Axial load-displacement curves for each microspine are compared to linear model predictions in Fig. 5d, showing agreement at small displacements to within 20%. Table I provides the percent error between the predicted stiffness k_a and the measured stiffness \hat{k}_a over the first 0.5mm of extension. While the assumptions of this linear model do not apply to large displacements, we see that the relative stiffness ordering of the four designs remains unchanged and all exhibit similar nonlinearity. Thus by matching the predicted small-displacement stiffness designers can still generate designs that produce similar forces at large displacements. The predicted normal stiffness values were less accurate than the axial predictions. For the normal flexures in particular, small amounts of preload in the test setup could have had a large effect on the measured stiffness values.

Despite these limitations, the model is effective at comparing relative axial stiffness between different SDM and

TABLE I
MICROSPINE MODEL PARAMETERS AND VALIDATION

Parameter	SDM	FDM 1	FDM 2	FDM 3
E , MPa	2	26	26	26
h , mm	1.5	1.6	1.6	1.6
θ	79°	79°	79°	79°
r_1 , mm	14.5	14.5	14.5	14.5
r_2 , mm	30.0	30.0	30.0	30.0
L_s , mm	6.5	4.3	4.3	4.3
w_s , mm	3.0	0.9	0.9	0.9
n_s	1	2	2	2
L_a , mm	4.0	9.0	8.4	8.4
w_a , mm	4.5	1.5	1.9	2.3
R_a , mm	-	1.5	1.4	1.4
l_a , mm	-	0.3	0.1	0.5
α_a	-	0°	0°	-15°
S_a	1	0.076	0.156	0.334
L_n , mm	33.0	30.8	30.8	30.8
w_n , mm	0.8	1.1	1.1	1.1
R_n , mm	-	0.8	0.8	0.8
l_n , mm	-	1.7	1.7	1.7
α_n	-	0°	0°	0°
S_n	1	0.030	0.030	0.030
k_{axial} , N/mm	3.71	1.89	2.84	5.19
\hat{k}_{axial} , N/mm	3.35	2.28	2.52	4.64
Error, %	20.4	-11.2	-10.7	-9.7

FDM designs despite very different material properties and flexure geometries. Using this model enables designers of new FDM microspines to optimize their suspension geometry appropriately given an expected change in tensile modulus to maintain the desired microspine compliance.

IV. EXPERIMENTAL METHODS

Relative performance of the three manufacturing methods was evaluated through tests simulating the loading experienced by a microspine during use in a gripper. Mechanical properties of each microspine type were evaluated using an Universal Testing machine (Instron 5969, 1 kN load cell). These included the microspine stiffness in the axial direction, the stiffness in the normal direction, the maximum axial load before the microspine suffers permanent damage, the observed failure mechanism, and the effect of fatigue measured by the decrease in required axial force to cause the same amount of displacement. For the microspine stiffness characterization (both axial and normal direction) the loading velocity was 5 mm/min and for the fatigue test, 100 cycles were performed with a 5 mm/min loading and unloading cycle. Five microspines of each type were tested for axial and tangential stiffness and axially loaded to failure. The FDM microspines that were measured correspond to the FDM 2 design above. In addition, one SDM and one FDM microspine were each subjected to cyclic axial loading. Only two of the five HDM microspines were able to reach a displacement of 5mm before failure, so an HDM microspine was not included in this test.

During load testing, microspines were constrained as they would be in practice when incorporated into a gripper. Separate fixtures were used to support microspines during axial and normal loading, as shown in Fig. 6. In each case, the microspine was translationally constrained relative to the

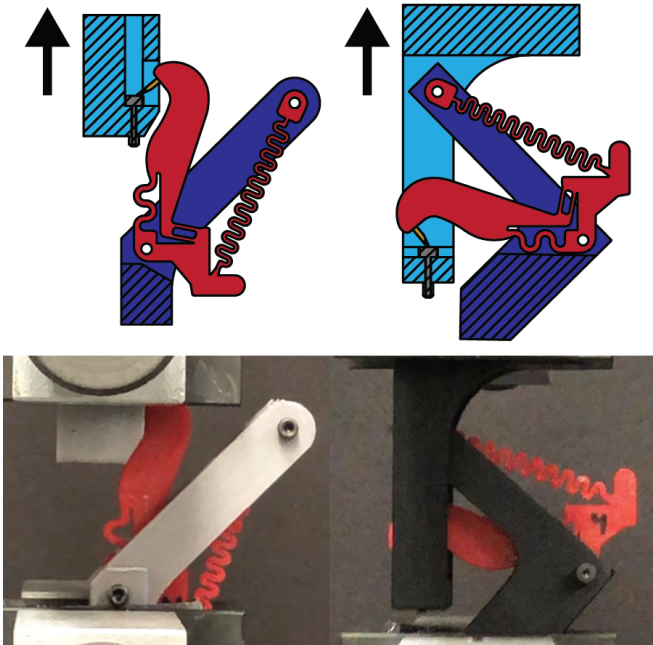


Fig. 6. Experimental setup for measurement of microspine axial stiffness (left) and normal stiffness (right). The top diagrams show a section view of each assembly, where the upper fixture is in light blue and the lower fixture is in dark blue. The bottom images show the test assemblies with the microspine unloaded.

lower fixture at the two pivots. A socket-head bolt in the upper fixture was used to securely engage the hook tip.

V. RESULTS AND DISCUSSION

The measured mechanical properties of microspines manufactured with each method are summarized in Table II. The stiffness measurements for both axes were based on measured load at 6mm of displacement (leaving out any samples that failed early).

The axial load-displacement curves for each microspine type are shown in Fig. 7, left, averaged across the five samples. A Butterworth filter was used to smooth out the data during post-processing. We see very close agreement between all three microspine types, with HDM microspines 15.5% stiffer than SDM and FDM microspines 11.3% less stiff than SDM. The agreement between the HDM and SDM microspines is to be expected because both microspines use the same flexure geometry and flexible material. However, the agreement between the SDM and FDM microspine results from deliberate tuning of the FDM microspine's serpentine flexure geometry.

The FDM microspines also exhibit a more linear load-displacement curve, possibly due to the serpentine flexure geometry or the material properties of the filament. The non-linearity of the SDM curve is slightly beneficial for load-sharing at larger displacements, because differences in displacement between microspines have less effect on their relative forces, but the effect is small enough to be negligible.

Similarly, Fig. 7, right, shows agreement between the normal stiffness of all three microspine types for most of the

TABLE II
EXPERIMENTAL COMPARISON OF MECHANICAL PROPERTIES

Measurement	SDM	HDM	FDM
Axial stiffness, N/mm	2.31 ± 0.29	2.67 ± 0.43	2.05 ± 0.06
Normal stiffness, N/mm	0.028 ± 0.004	0.033 ± 0.005	0.022 ± 0.005
Maximum load, N	$15.9 \pm 2.1^*$	10.9 ± 8.0	41.1 ± 2.1
Force decrease, 100 cycles, N	2.36 (17.4%)	-	1.30 (12.4%)

*Maximum load for SDM microspines is typically around 30N.

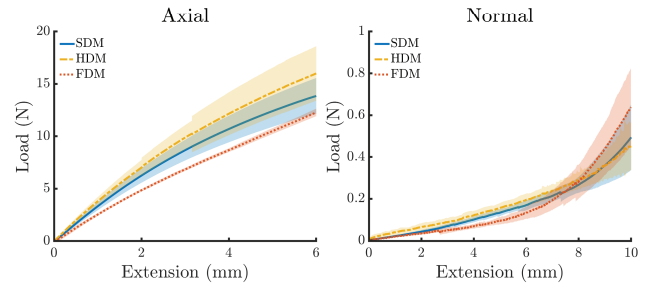


Fig. 7. Overlaid axial (left) and normal (right) load-displacement curves for each of the measured microspine designs. Shaded regions indicate one standard deviation. Samples are removed from the averaging after a failure occurs, causing small discontinuities in the HDM axial load. Small discontinuities in the FDM normal load plot were caused by slight shifting of the hook relative to the fixture.

measured range, with HDM microspines 14.9% stiffer than SDM and FDM microspines 21.4% less stiff than SDM. At very large displacements, the normal stiffness of the FDM microspines begins to sharply increase, as the microspine collides with the normal flexure above. While this also occurs for SDM and HDM microspines, the FDM flexures have significantly higher bending stiffness and therefore this interference has a much greater effect. As this interference only occurs near the limit of travel the actual impact on performance is minor in most circumstances.

With further tuning of the serpentine flexure geometry, both the average axial and normal stiffness of the FDM microspines could be made to match the SDM microspines arbitrarily well. In practice, the optimal microspine stiffness is dependent on the distribution of surface asperities, terrain roughness, expected load, and number of microspines in the gripper, so further optimization of the microspine stiffness should be done with a specific application in mind.

In Fig. 8, results are shown for each sample being axially loaded to failure. The SDM samples failed at 13-19N, due to either delamination (3 samples) or a break in the rigid material (2 samples). We later obtained original SDM microspine samples from the authors of [10] and determined that their failure load was significantly higher at around 30N, although their stiffness properties were identical. This suggests that a defect occurred during our manufacturing process, and highlights the advantage of easier and more consistent fabrication using the FDM process compared to SDM. HDM microspine performance is much less reliable, with delamination at the urethane-PLA interface occurring anywhere from 0-19N. We attribute this to poor adhesion

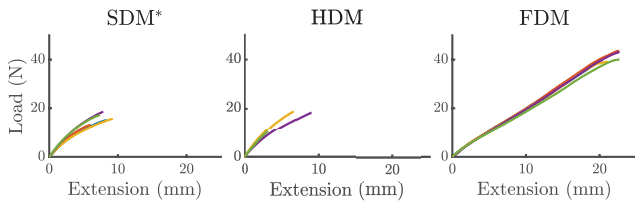


Fig. 8. Stress-strain curves of individual SDM* (left), HDM (center), and FDM (right) samples when axially loaded until failure. One HDM sample evidently delaminated during the mold wall removal process prior to the experiment, and so was not included in the plot. *The maximum load for SDM microspines is typically around 30N.

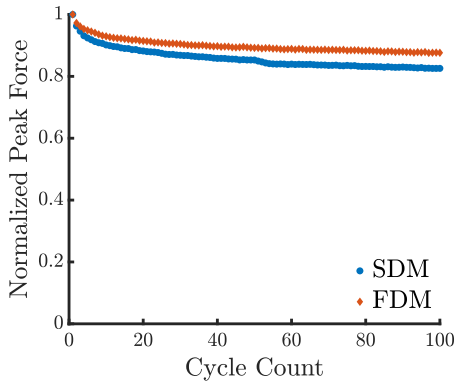


Fig. 9. Maximum force reached during each load cycle normalized by the force at the first loading cycle, plotted over 100 load cycles with a 5mm displacement for both SDM and FDM microspines.

between the flexible urethane and PLA materials relative to the adhesion between the flexible and rigid urethane resins. The FDM samples are consistently able to reach around 40N of applied load, at which point angular deflection of the microspine allows the hook to slip out of the bolt head. The microspine itself is left intact, so the maximum load before material failure is even greater. This superior performance is due to the use of a single material, which avoids the failure mode of delamination. Additionally, the Cheetah material has a much higher tensile strength than the flexible urethane (39MPa vs 6MPa respectively) which allows FDM microspines to support larger loads before rupture.

Fatigue testing results are shown in Fig. 9. For each microspine, the peak load reached during each cycle is plotted against the number of elapsed cycles. The peak load measurements are normalized by the peak load of the first cycle for that microspine. The SDM microspine exhibits a 17.4% reduction in force over 100 cycles, compared to a 12.4% reduction for the FDM microspine. These results suggest that FDM microspine performance degrades more gradually with use than that of SDM microspines. For reference, wear of the spine tip is known to occur over a comparable time scale (the tip radius levels off after around 50 cycles) [10].

As a final validation, nine FDM microspines were assembled into a simple gripper (Fig 1), which was placed against a cinder block surface and tangentially loaded until

disengagement. The gripper was able to consistently support a 30N tangential load before adhesion failure, with the individual microspines visibly displacing to catch on asperities as expected.

Overall, these results demonstrate that FDM microspines can achieve comparable stiffness properties to SDM microspines while providing increased durability in the form of a higher maximum load, better maintenance of mechanical properties after cyclic loading, and fewer failure modes. We conclude that microspines fabricated using this new approach are able to match the adhesive performance of existing SDM microspines, as also demonstrated by hand-held gripper tests.

FDM microspines offer a number of advantages beyond their mechanical properties. Foremost is the reduction in production time. Manufacturing a batch of 25 microspines through SDM requires 2-3 hours of machining time, with a similar amount required for setup and cleanup. The hook preparation, casting, and mold removal steps combined required an additional 1-2 hours. However, the bulk of the time is the curing process, which requires 1 hour for the rigid polymer and 16 hours for the flexible polymer. The total comes out to around 24 hours or 1 hour per microspine, of which 4 hours or 10 minutes per microspine actively requires human labor. In contrast, a batch of 9 FDM microspines requires 2 hours of printing and 10 minutes of hook preparation, for an average of 15 minutes per microspine, of which only 1 minute of human labor is required. This difference becomes even more drastic for small batches – the machining setup and curing times for SDM are unchanged, so manufacturing a single microspine still requires 2-3 hours of human effort and an overnight casting process. In contrast, manufacturing a single FDM microspine can be done in 15 minutes.

The SDM process also requires users to learn a complicated casting process with many opportunities for error, while setting up the FDM process can be as simple as downloading a gcode file. Other advantages include the shelf life of the materials; once opened, the urethane resins begin to harden and lose efficacy, while the flexible filament is much more stable. Lastly, the SDM process requires access to a CNC mill, fume hood, and vacuum chamber, while the FDM process uses only a basic 3D printer.

VI. CONCLUSION AND FUTURE WORK

FDM microspines provide a convenient alternative to SDM in situations where rapid iteration is desired, access to CNC machining and other equipment is limited, relatively small numbers of microspines are needed, or microspines are at risk of being overloaded. SDM microspines remain viable in cases where tight dimensional tolerances are necessary, or when large quantities of microspines are needed and durability is not a concern. For example, FDM is ideal for rapid prototyping of new microspine designs, as is necessary when developing a novel gripper or adapting a microspine design to a particular climbing substrate. During climbing, FDM microspines can support greater loads without the need for overload protection mechanisms. The simplicity of the

FDM process also increases the accessibility of microspine technology, making it easier for researchers in other areas to augment their robots with climbing or perching capabilities.

This work leaves open several directions for further study. One unaddressed question is how FDM and SDM microspines compare in terms of shelf life and temperature tolerance. SDM microspines tend to degrade over time even while not in use due to UV exposure, while the performance of FDM microspines over a long time horizon has not yet been investigated. Similarly, it is not yet known which method offers better performance at either high or low temperature extremes. There is also room for further innovation on the design of FDM microspines, for instance by exploiting the ability of FDM to produce overhanging features, by embedding additional components besides the hook to provide structural or other benefits like sensing, or by designing new flexure geometries to provide more effective load-displacement profiles as the microspine is loaded. Another area for exploration is the adaptation of this single-material microspine design to other manufacturing processes that work with flexible materials, such as laser cutting, casting, or injection molding. These approaches may allow the use of materials with superior mechanical characteristics or enable efficient mass-production of large quantities of microspines. Finally, further experimentation with different material combinations may allow HDM microspines to overcome their delamination issues and become equally viable.

REFERENCES

- [1] I. Baldwin, S. Kenig, A. Nicholas *et al.*, “Extreme science: Exploring the use of extreme-terrain rovers in Mars sample return,” in *IEEE Aerospace Conference*, 2016, pp. 1–11.
- [2] S. W. Squyres, A. H. Knoll, R. E. Arvidson *et al.*, “Exploration of Victoria Crater by the Mars rover Opportunity,” *Science*, vol. 324, no. 5930, pp. 1058–1061, 2009.
- [3] R. J. L evell e and S. Datta, “Lava tubes and basaltic caves as astrobiological targets on Earth and Mars: A review,” *Planetary and Space Science*, vol. 58, no. 4, pp. 592 – 598, 2010.
- [4] I. A. Nesnas, L. Kerber, A. Parness *et al.*, “Moon Diver: a discovery mission concept for understanding the history of secondary crusts through the exploration of a lunar mare pit,” in *IEEE Aerospace Conference*, 2019, pp. 1–23.
- [5] M. Spenko, “Making contact: A review of robotic attachment mechanisms for extraterrestrial applications,” *Advanced Intelligent Systems*, p. 2100063, 2022.
- [6] A. Parness, M. Frost, N. Thatte *et al.*, “Gravity-independent rock-climbing robot and a sample acquisition tool with microspine grippers,” *Journal of Field Robotics*, vol. 30, no. 6, pp. 897–915, 2013.
- [7] A. Parness, N. Abcouwer, C. Fuller *et al.*, “LEMUR 3: A limbed climbing robot for extreme terrain mobility in space,” in *IEEE International Conference on Robotics and Automation*, 2017, pp. 5467–5473.
- [8] A. T. Asbeck, S. Kim, W. R. Provancher *et al.*, “Scaling hard vertical surfaces with compliant microspine arrays,” *Robotics Science and Systems Conference*, 2005.
- [9] M. J. Spenko, G. C. Haynes, J. A. Saunders *et al.*, “Biologically inspired climbing with a hexapedal robot,” *Journal of Field Robotics*, vol. 25, no. 4-5, pp. 223–242, 2008.
- [10] S. Backus, J. Izraelevitz, J. Quan *et al.*, “Design and testing of an ultralight weight perching system for sloped or vertical rough surfaces on Mars,” in *IEEE Aerospace Conference*, 2020, pp. 1–12.
- [11] K. Carpenter, N. Wiltsie, and A. Parness, “Rotary microspine rough surface mobility,” *IEEE/ASME Transactions on Mechatronics*, vol. 21, no. 5, pp. 2378–2390, 2016.
- [12] A. Asbeck, S. Kim, A. McClung, and A. Parness, “Climbing walls with microspines,” *IEEE International Conference on Robotics and Automation*, 2006.
- [13] T. Wallin, J. Pikul, and R. Shepherd, “3D printing of soft robotic systems,” *Nature Reviews Materials*, vol. 3, no. 6, p. 84, 2018.
- [14] R. Merz, F. Prinz, K. Ramaswami *et al.*, “Shape deposition manufacturing,” in *International Solid Freeform Fabrication Symposium*, 1994.
- [15] L. Weiss, R. Merz, F. Prinz *et al.*, “Shape deposition manufacturing of heterogeneous structures,” *Journal of Manufacturing Systems*, vol. 16, no. 4, pp. 239–248, 1997.
- [16] S. Y. Wu, C. Yang, W. Hsu, and L. Lin, “3D-printed microelectronics for integrated circuitry and passive wireless sensors,” *Microsystems and Nanoengineering*, vol. 1, 2015.
- [17] T. D. Ngo, A. Kashani, G. Imbalzano *et al.*, “Additive manufacturing (3D printing): A review of materials, methods, applications and challenges,” *Composites Part B: Engineering*, vol. 143, pp. 172–196, 2018.
- [18] R. H. Sanatgar, A. Cayla, C. Campagne, and V. Nierstrasz, “Morphological and electrical characterization of conductive polylactic acid based nanocomposite before and after FDM 3D printing,” *Journal of Applied Polymer Science*, vol. 136, no. 6, p. 47040, 2019.
- [19] C. Tawk, Y. Gao, R. Mutlu, and G. Alici, “Fully 3D printed monolithic soft gripper with high conformal grasping capability,” in *IEEE/ASME International Conference on Advanced Intelligent Mechatronics*, 2019, pp. 1139–1144.
- [20] P. R. Kuppens, M. A. Bessa, J. L. Herder, and J. B. Hopkins, “Compliant mechanisms that use static balancing to achieve dramatically different states of stiffness,” *Journal of Mechanisms and Robotics*, vol. 13, no. 2, 01 2021.
- [21] R. R. Ma, J. T. Belter, and A. M. Dollar, “Hybrid deposition manufacturing: Design strategies for multimaterial mechanisms via three-dimensional printing and material deposition,” *Journal of Mechanisms and Robotics*, vol. 7, no. 2, 05 2015.
- [22] E. G. Merriam, A. B. Berg, A. Willig *et al.*, “Microspine gripping mechanism for asteroid capture,” in *Aerospace Mechanisms Symposium*, 2016.
- [23] A. Parness, A. Willig, A. Berg *et al.*, “A microspine tool: Grabbing and anchoring to boulders on the asteroid redirect mission,” in *IEEE Aerospace Conference*, 2017, pp. 1–10.
- [24] A. Parness, T. Evans, W. Raff *et al.*, “Maturing microspine grippers for space applications through test campaigns,” *AIAA SPACE and Astronautics Forum and Exposition*, no. 203999, pp. 1–17, 2017.
- [25] M. Martone, C. Pavlov, A. Zeloof *et al.*, “Enhancing the vertical mobility of a robot hexapod using microspines,” arXiv, Tech. Rep. arXiv:1906.04811 [cs.RO], 2019.
- [26] R. J. Wallace, C. Pavlov, and A. Johnson, “Design of microspine-enhanced spring legs for robotic running and climbing,” in *Dynamic Walking*, May 2020.
- [27] B. D. Miller, P. R. Rivera, J. D. Dickson, and J. E. Clark, “Running up a wall: the role and challenges of dynamic climbing in enhancing multi-modal legged systems,” *Bioinspiration & biomimetics*, vol. 10, no. 2, p. 025005, 2015.
- [28] S. B. Backus, R. Onishi, A. Bocklund *et al.*, “Design and testing of the JPL-Nautilus gripper for deep-ocean geological sampling,” *Journal of Field Robotics*, vol. 37, no. 6, pp. 972–986, 2020.
- [29] S. Wang, H. Jiang, and M. R. Cutkosky, “Design and modeling of linearly-constrained compliant spines for human-scale locomotion on rocky surfaces,” *The International Journal of Robotics Research*, vol. 36, no. 9, pp. 985–999, 2017.
- [30] S. Yang, S. Qiao, and N. Lu, “Elasticity solutions to nonbuckling serpentine ribbons,” *Journal of Applied Mechanics*, vol. 84, no. 2, 11 2016.
- [31] J. B. Hopkins and M. L. Culpepper, “Synthesis of multi-degree of freedom, parallel flexure system concepts via freedom and constraint topology (FACT)–Part I: Principles,” *Precision Engineering*, vol. 34, no. 2, pp. 259–270, 2010.
- [32] H. Somarathna, S. Raman, D. Mohotti *et al.*, “Hyper-viscoelastic constitutive models for predicting the material behavior of polyurethane under varying strain rates and uniaxial tensile loading,” *Construction and Building Materials*, vol. 236, p. 117417, 2020.
- [33] S. Awtar, A. H. Slocum, and E. Sevincer, “Characteristics of beam-based flexure modules,” *Journal of Mechanical Design*, vol. 129, no. 6, pp. 625–639, 05 2006.